Robust gapless superconductivity in 4Hb-TaS$_2$

David Dentelski ●,[1,2] Ezra Day-Roberts ●,[3] Turan Birol ●,[4] Rafael M. Fernandes,[3] and Jonathan Ruhman ●[1,2]

[1]*Department of Physics, Bar-Ilan University, 52900 Ramat Gan, Israel*
[2]*Center for Quantum Entanglement Science and Technology, Bar-Ilan University, 52900 Ramat Gan, Israel*
[3]*School of Physics and Astronomy, University of Minnesota, Minneapolis, Minnesota 55455, USA*
[4]*Department of Chemical Engineering and Materials Science, University of Minnesota, Minneapolis, Minnesota 55455, USA*

The superconducting transition metal dichalcogenide (TMD) 4Hb-TaS$_2$ consists of alternating layers of H and T structures, which in their bulk form are metallic and Mott insulating, respectively. Recently, this compound has been proposed as a candidate chiral superconductor, due to an observed enhancement of the muon-spin relaxation at T_c. 4Hb-TaS$_2$ also exhibits a puzzling T-linear specific heat at low temperatures, which is unlikely to be caused by disorder. Elucidating the origin of this behavior is an essential step in discerning the true nature of the superconducting ground state. Here, we propose a simple model that attributes the T-linear specific heat to the emergence of a robust multiband gapless superconducting state. We show that an extended regime of gapless superconductivity naturally appears when the pair-breaking scattering rate on distinct Fermi-surface pockets differs significantly, and the pairing interaction is predominantly intrapocket. Using a tight-binding model derived from first-principle calculations, we show that the pair-breaking scattering rate promoted by slow magnetic fluctuations on the T layers, which arise from proximity to a Mott transition, can be significantly different in the various H-layer dominated Fermi pockets depending on their hybridization with T-layer states. Thus, our results suggest that the ground state of 4Hb-TaS$_2$ consists of Fermi pockets displaying gapless superconductivity, which are shunted by superconducting Fermi pockets that are nearly decoupled from the T layers.

I. INTRODUCTION

The observation of superconductivity in transition metal dichalcogenides (TMD), including in monolayer form, has recently spurred significant interest from the community [1–10]. Among them, bulk 4Hb-TaS$_2$ has emerged as a possible unconventional superconductor. Recent muon-spin rotation (μSR) measurements performed on 4Hb-TaS$_2$ reveal a slight enhancement of the relaxation rate, which onsets at the superconducting transition temperature T_c [11]. The authors (including one of us) have interpreted this signal as evidence of chiral superconductivity. However, recent nuclear magnetic resonance measurements performed on Sr$_2$RuO$_4$, a candidate chiral superconductor that exhibits such a muon-relaxation enhancement, are inconsistent with the $p + ip$ chiral order parameter [12,13]. Indeed, one may consider alternative mechanisms that tie such a weak enhancement of the muon relaxation to the onset of superconductivity, e.g., if local magnetic moments are present, which are screened in the metallic state but not below T_c. For this reason, it is essential to understand the correct microscopic model and corresponding ground state of superconducting 4Hb-TaS$_2$.

4Hb-TaS$_2$ is a TMD comprised of alternating single layers with 1T and 1H structures (see Fig. 1). At low temperature, bulk 1T-TaS$_2$ is a strongly correlated insulator due to the small bandwidth associated with a nearly flat conduction band. This flatband results from the reconstruction of the band structure by a prior transition into a "star-of-David" charge-density wave (CDW) state [1]. Interestingly, the insulating 1T compound fails to order magnetically to the lowest measured temperatures [14], which has motivated the proposal that it may be a spin liquid [15–17] or a dimerized band insulator [18]. The 2H polymorph also undergoes a CDW transition, but with a different structure. As opposed to the 1T polymorph, it remains a metal, which is characterized by multiple Fermi pockets. At $T_c^{2H} = 0.7$ K it undergoes a superconducting transition.

ARPES measurements performed on the 4Hb polymorph show that the star-of-David CDW still forms in the 1T layer [11]. However, there is no signature of the insulating state to the lowest measurable temperatures [19]. Instead, the entire compound becomes superconducting at $T_c^{4Hb} = 2.7$ K [11], which is elevated when compared to bulk 2H-TaS$_2$, but still smaller than exfoliated single layer [3,7] or intercalated samples [20]. Thus, the 4Hb compound intrinsically couples highly-itinerant and nearly localized electrons, a situation that is interesting on its own [21].

A puzzling experimental observation, which may shed light on the ground state properties of 4Hb-TaS$_2$, is the linear in T behavior of the specific heat at low temperatures inside the superconducting state. While the specific heat near the transition temperature T_c^{4Hb} resembles that of a fully gapped s-wave superconductor, the low-temperature behavior resembles that of a metal, with a Sommerfeld coefficient value that
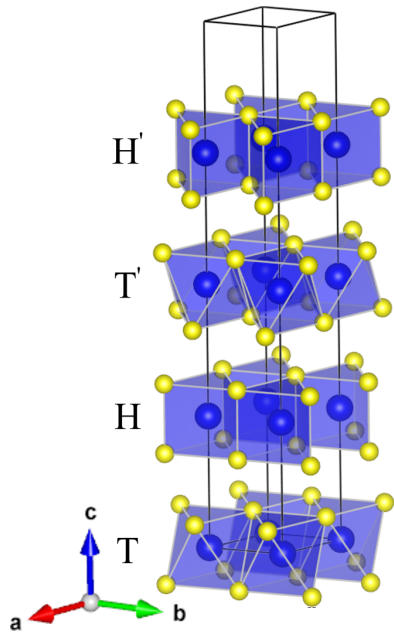
FIG. 1. Crystal structure of $4Hb$-TaS$_2$. The unit cell consists of four layers of Ta atoms with alternating trigonal (H) and octahedral (T) coordination. Each layer is a triangular lattice of Ta atoms.

is 15% of the normal state value [11]. We also note that similar anomalies in the specific heat have been observed in other candidate chiral superconductors, such as the heavy-fermion compound UTe$_2$ [22] and La$_7$Ni$_3$ [23].

The simplest possible explanation for the T-linear behavior of the specific heat would be the existence of a sizable nonsuperconducting volume fraction due to inhomogeneities or impurities even below T_c. However, this is unlikely to be the sole explanation, given the sharp superconducting transition and homogeneous diamagnetic response seen in scanning superconducting quantum interference device (SQUID) measurements [24]. A more exotic explanation would be the emergence of Bogoliubov Fermi surfaces, which are known to arise from time-reversal symmetry breaking in nodal superconductors [25] or from pure pair-density wave states. However, before reaching the linear-in-T behavior, the specific heat decays exponentially rather than in a power-law fashion, which is inconsistent with Bogoliubov Fermi surfaces, which are "inflated" line or point nodes [25] (see Appendix B). Another option is that strong pair-breaking disorder is present, filling the gap with electronic states. Such a gapless state was predicted by Abrikosov and Gor'kov in their seminal work [26]. However, in the standard Abrikosov-Gor'kov theory for single-band superconductors, this gapless superconducting state appears only in a very narrow range of the pair-breaking scattering rate, just before superconductivity is completely destroyed by disorder. Moreover, this state is also characterized by a smeared transition and by the absence of coherence peaks in the density of states [27,28].

In this paper, we apply Abrikosov-Gor'kov theory to the case of two-band superconductors with dominant intraband pairing interaction. We show that gapless superconductivity naturally emerges over a much wider range of pair-breaking scattering rates when the disorder potential is significantly

larger on one of the Fermi pockets. Using a two-band toy model with these characteristics, we are able to reproduce the temperature dependence of the specific heat data of $4Hb$-TaS$_2$, including the T-linear behavior, over a wide range of pair-breaking scattering rates.

To demonstrate the relevance of this simple model to $4Hb$-TaS$_2$, we performed *ab initio* band structure calculations and derived a simplified tight-binding model using the maximally localized Wannier functions. The Fermi surface consists of several pockets centered at the high-symmetry points of the Brillouin zone. While the spectral weights of the pockets centered at Γ and K are dominated by the H-layer states, the M-centered pockets have large contributions from the T-layer states. Around each of these high-symmetry points, the Fermi pockets come in pairs—except at the boundaries of the Brillouin zone at $k_z = \pm\pi/c$, where a screw symmetry makes all bands fourfold degenerate. Since the $2H$ polymorph superconducts on its own, we associate a pair of pockets with dominant H-layer character in $4Hb$-TaS$_2$ to the two bands in our toy model.

The key point is that one of the pockets in each of these pairs hybridizes much more strongly with the T-layer states, particularly at the zone center plane ($k_z = 0$). Now, the $1T$ polymorph on its own is a Mott insulator with presumably strong (but possibly frustrated) magnetic fluctuations arising from local moments. Low-energy, slow magnetic fluctuations are expected to have a pair-breaking effect [29,30], which shares some similarities with the pair-breaking effect of magnetic impurities. Therefore, the pocket in the pair that is most strongly hybridized with the T-layer states is expected to be subjected to a stronger pair-breaking potential. We demonstrate that this is indeed the case by computing the scattering rate for each Fermi pocket after modeling the slow magnetic fluctuations as local magnetic "impurity" scatterers in the T layer. The scattering rates in each pocket of the same pair is notably different near the $k_z = 0$ plane, which qualitatively justifies the assumptions of our toy model. Additionally, we observe a significant difference in the scattering strength between the Γ and K pockets, where the former is larger. Overall, our results suggest that the ground state of $4Hb$-TaS$_2$ is a combination of gapless Fermi pockets and fully gapped superconducting pockets, which does not necessarily break time-reversal symmetry.

The rest of this paper is organized as follows. In Sec. II we present our two-band toy model, where we assume that only one of the bands is coupled strongly to magnetic moments originated in the T layer. We show that within this model, gapless superconductivity naturally emerges over a wide range of pair-breaking scattering rates. To relate our model to the microscopic properties of $4Hb$-TaS$_2$, in Sec. III we construct a tight-binding model for this compound. We find that our assumptions of the different coupling to T-layer magnetic moments holds at $k_z = 0$, where we can expect local moments on the T layer to couple much weaker to the inner Fermi surfaces in comparison to the outer ones. In Sec. IV we use these results to numerically estimate the scattering rate on the inner and outer Fermi surfaces. Section V summarizes our results and discusses the limitations and implication of our model to understand the superconducting state of $4Hb$-TaS$_2$.

II. ROBUST GAPLESS SUPERCONDUCTIVITY IN A TWO-BAND TOY MODEL

In this section we present a simple toy model to explain the emergence of robust gapless superconductivity in $4Hb$-TaS$_2$. We show that such a state is stabilized over a wide range of parameters when one of the two Fermi pockets couples strongly to pair-breaking disorder, while the other one is only weakly coupled.

A. Self-consistent gap equation

We consider the simplest possible scenario of two pockets (labeled 1 and 2) with zero center-of-mass momentum pairing, which are described by the Gor'kov Green's function

$$\mathcal{G}_0(\mathbf{k}, i\omega_n) = \begin{pmatrix} G_1(\mathbf{k}, i\omega_n) & 0 \\ 0 & G_2(\mathbf{k}, i\omega_n) \end{pmatrix}, \qquad (1)$$

written in the Nambu space $\Psi_{\boldsymbol{k}} = (c_{\boldsymbol{k}\uparrow 1}^\dagger, c_{-\boldsymbol{k}\downarrow 1}, c_{\boldsymbol{k}\uparrow 2}^\dagger, c_{-\boldsymbol{k}\downarrow 2})$, where

$$G_j(\mathbf{k}, i\omega_n) = -\frac{i\omega_n\tau^0 + \xi_{\mathbf{k},j}\tau^3 + \Delta_j\tau^1}{\omega_n^2 + \xi_{\mathbf{k},j}^2 + \Delta_j^2}. \qquad (2)$$

Here, τ^α are Pauli matrices in the particle-hole basis, $\xi_{\mathbf{k},j}$ is the dispersion relation of band $j = 1, 2$ which we assumed to be spherically symmetric, $\omega_n = 2\pi k_B T(n + 1/2)$ are the fermionic Matsubara frequencies, and T is the temperature. For simplicity, we assume s-wave pairing, although our main result should hold for any *nodeless* gap function (including a chiral state in two dimensions).

To determine the magnitude of the superconducting order parameter Δ_j within Abrikosov-Gor'kov (AG) theory, we first incorporate the effect of disorder by computing the self-energy correction to the Gor'kov Green's function

$$\Sigma(\mathbf{k}, i\omega_n) = n_{\mathrm{imp}} \int \frac{d^3 p}{(2\pi)^3} \widehat{\mathbf{V}}_{\mathbf{p}-\mathbf{k}} \, \mathcal{G}(\mathbf{p}, i\omega_n) \, \widehat{\mathbf{V}}_{\mathbf{k}-\mathbf{p}}, \qquad (3)$$

where $\mathcal{G}^{-1} = \mathcal{G}_0^{-1} - \Sigma$ is the dressed Green's function. This correction is obtained following the standard AG theory, where we average over uncorrelated configurations of point-like defects with concentration n_{imp}. We assume that the source of pair-breaking is magnetic disorder in the T layers. This leads to the Nambu-space disorder-potential matrix

$$\widehat{\mathbf{V}} = \begin{pmatrix} V_1 & 0 & V_{12} & 0 \\ 0 & V_1 & 0 & V_{12} \\ V_{12} & 0 & V_2 & 0 \\ 0 & V_{12} & 0 & V_2 \end{pmatrix}. \qquad (4)$$

Here V_1, V_2, and V_{12} are the intra- and interband disorder-potential strengths, respectively. In what follows we assume $V_1, V_{12} \ll V_2$, which implies that band 2 is coupled much stronger to the magnetic impurities than band 1. We will show that in this limit, gapless superconductivity is stabilized over a wide range of parameters. For simplicity, however, let us consider the extreme limit where $V_1 = V_{12} = 0$ and $V_2 \neq 0$.

In this case, the block of the Green's function corresponding to band 1 retains its form in Eq. (2), while the block of band 2 needs to be calculated self-consistently using Eq. (3). The solution is obtained by substituting, in the Green's function expression in

Eq. (2), $\Delta_2 \rightarrow \tilde{\Delta}_2 = \Delta_2 - \Gamma\tilde{\Delta}_2/(2\sqrt{\tilde{\omega}_n^2 + \tilde{\Delta}_2^2})$ and $\omega_n \rightarrow \tilde{\omega}_n = \omega_n + \Gamma\tilde{\omega}_n/(2\sqrt{\tilde{\omega}_n^2 + \tilde{\Delta}_2^2})$. Here, $\Gamma = 2\pi V^2 n_{\mathrm{imp}} \nu_2^0$ is the pair-breaking scattering rate and ν_2^0 is the density of states of band 2 at the absence of superconductivity. These equations can be written in a concise manner by defining $x_n = \tilde{\Delta}_2/\tilde{\omega}_n$ and dividing them by one another, such that

$$x_n = \frac{\Delta_2 - \Gamma |x_n|/(2\sqrt{1 + x_n^2})}{\omega_n + \Gamma \mathrm{sgn}(\omega_n)/(2\sqrt{1 + x_n^2})}. \qquad (5)$$

We are now in position to determine the magnitude of Δ_j from the gap equation using the dressed Green's function

$$\begin{pmatrix} \Delta_1 \\ \Delta_2 \end{pmatrix} = \pi k_B T \sum_{|\omega_n| < \omega_D} \begin{pmatrix} \lambda_1 & u \\ u & \lambda_2 \end{pmatrix} \begin{pmatrix} \frac{\Delta_1}{\sqrt{\omega_n^2 + \Delta_1^2}} \\ \frac{\tilde{\Delta}_2}{\sqrt{\tilde{\omega}_n^2 + \tilde{\Delta}_2^2}} \end{pmatrix}, \qquad (6)$$

where λ_j and u are dimensionless intraband and interband pairing couplings, respectively, and the summation is cut off at Debye frequency ω_D.

Equations (5) and (6) can be readily solved numerically by iteration. However, it is also helpful to obtain asymptotic solutions in the limits $x_n \gg 1$, corresponding to weak disorder and small frequency, and $x_n \ll 1$, corresponding to strong disorder and large frequency.

In the regime $x_n \gg 1$ we find the asymptotic solution:

$$x_n \sim \frac{\Delta_2 - \Gamma}{\omega_n}, \qquad \omega_n \rightarrow 0. \qquad (7)$$

This equation reflects the well-known result in AG theory that the critical scattering rate above which gapless superconductivity emerges is given by $\Gamma_* = \Delta_2$, which is slightly smaller than the critical value Γ_c for which superconductivity is destroyed (i.e., when Δ_2 goes to zero). In what follows, we will show explicitly via a computation of the density of states (DOS) that $\Gamma_* = \Delta_2$ indeed implies a finite DOS at the Fermi level and, therefore, gapless superconductivity.

On the other hand, for $x_n \ll 1$, the asymptotic solution is given by

$$x_n \sim \frac{\Delta_2 \mathrm{sgn}(\omega_n)}{|\omega_n| + \Gamma}, \qquad \Delta_2/\Gamma \ll 1. \qquad (8)$$

Note that this solution becomes asymptotically exact in the limit $\Delta_2 \ll \Gamma$, which defines the strong disorder limit, and in the high frequency limit $\omega \rightarrow \infty$.

In both regimes, the value of Δ_2 is obtained from the self-consistent solution of the gap Eq. (6). In Fig. 2(a) we plot the value of the two gaps normalized by their bare value (i.e., obtained with $\Gamma = 0$) as a function of Γ for two cases, one with a finite but small interpocket pairing interaction $u = -0.035$ and $\lambda_1 = \lambda_2 = -0.17$ (solid lines), and one where $u = 0$ and $\lambda_1 = \lambda_2 = -0.2$ (dashed lines).

Let us first consider the latter case where there is no interpocket pairing. In this situation, Δ_1 is not affected by disorder, while Δ_2 is suppressed to zero very quickly. In agreement with AG theory, the gap vanishes slightly after reaching the gapless regime $\Delta_2 = \Gamma$ as predicted by Eq. (7) (which is marked by a yellow diamond in the figure).

On the other hand, when u is small but finite there is always a nonzero solution for Δ_2, which decreases monotonically with Γ. In particular, the region of gapless superconductivity
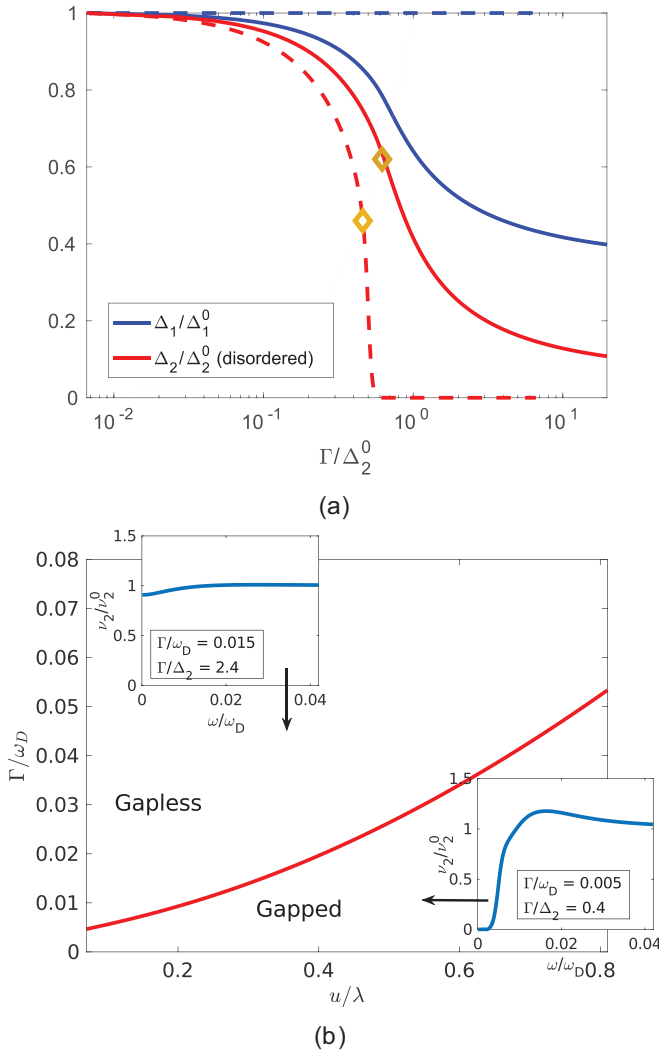
FIG. 2. (a) The superconducting order parameters Δ_1 and Δ_2, as a function of the pair-breaking rate Γ obtained from numerical solutions of Eqs. (5) and (6). The order parameters are normalized by their bare value $\Delta_{1,2}^0$, i.e., with no disorder ($\Gamma = 0$). The dashed lines represent the case of zero interpocket pairing $u = 0$ and $\lambda_1 = \lambda_2 = -0.2$. In this case, Δ_1 is unaffected by disorder while Δ_2 goes rapidly to zero. As a result, the region of gapless superconductivity, starting at the yellow diamond, is extremely narrow (the gray line is $\Delta_2 = \Gamma$ on a logarithmic scale). In contrast, the case of finite interpocket coupling $u = -0.035$ and $\lambda_1 = \lambda_2 = -0.17$ is represented by the solid lines. In this case, Δ_2 decreases slowly with Γ, resulting in a much wider region of gapless superconductivity. (b) The $\Gamma - u$ "phase diagram" that determines the conditions for gapless and gapped superconductivity in band 2. Note that the pair-breaking rate Γ is given in units of the Debye frequency ω_D, which serves as a upper cutoff in the gap equation, Eq. (6). The inset shows the corresponding density of states (DOS) of band 2 for two representative values of disorder, illustrating the gapped (bottom right) and gapless (top left) superconducting phases.

is extended to a much wider range of Γ values, starting from the value corresponding to the yellow diamond in Fig. 2(a) and extending all the way up. In Fig. 2(b), we present the corresponding "phase diagram" for gapped and gapless superconductivity in band 2 in the parameter space of Γ and

interpocket pairing u. The insets show the typical tunneling DOS ν_2/ν_2^0 of these two regions.

It should be noted that in any realistic system, band 1 will also be coupled to pair-breaking disorder, characterized by some rate Γ_1. It is also possible that interpocket pair-breaking Γ_{12} emerges in the case of non-pointlike impurities. The working hypothesis of this paper is that both pair-breaking scattering rates are much smaller than Γ. Based on our analysis above, and denoting the maximum of the two by $\max(\Gamma_1, \Gamma_{12}) = \delta\Gamma$, such that $\delta \ll 1$, we can conclude that robust gapless superconductivity appears in the wide regime $\Delta_2 < \Gamma < \Delta_1/\delta$.

Therefore, we have demonstrated that multipocket superconductors with disorder that couples much stronger to one pocket than the other exhibit gapless superconductivity over a wide range of disorder strengths. We now turn to discuss the experimental consequences of such a state, focusing on the specific heat.

B. Specific heat

The thermodynamic properties of the superconducting state is governed by the fermionic DOS. In the case of zero center-of-mass momentum pairing, the bands are decoupled at the single-particle level and contribute independently to the total density of states. The density of states of band 2 is given by

$$\frac{\nu_2(\omega)}{\nu_2^0} = -\frac{1}{\pi} \sum_{\mathbf{k}} \mathrm{Im} G_2^R(\mathbf{k}, \omega) = \mathrm{Re}\left[\frac{\omega}{\sqrt{\omega^2 - \mathcal{D}^2(\omega)}}\right], \quad (9)$$

where G_2^R is the retarded Green's function of band 2 obtained from analytical continuation and $\mathcal{D}(\omega)$ is the analytic continuation of

$$\mathcal{D}(i\omega_n) \equiv x_n \omega_n. \quad (10)$$

Similarly, the density of states of band 1 is given by $\nu_1(\omega)/\nu_1^0 = \mathrm{Re}[\omega/\sqrt{\omega^2 - \Delta_1^2}]$. Thus, the total density of states is $\nu(\omega) = \nu_1(\omega) + \nu_2(\omega)$.

It is clear from Eqs. (9) and (10) that when $x_n \omega_n = 0$, a finite density of states emerges at the Fermi level. Using Eq. (7), we see that this happens when $\Gamma = \Delta_2$. In the limit of strong disorder, $\Gamma \gg \Delta_2$, we can use Eq. (8) for band 2. Assuming that band 1 is fully gapped, we obtain a finite density of states at $\omega \to 0$ given by

$$\nu(\omega) \sim \frac{\nu_2^0}{\sqrt{1 + (\Delta_2/\Gamma)^2}}, \quad \omega \to 0 \quad (11)$$

which leads to a finite Sommerfeld coefficient $\gamma_N = \pi^2 k_B \nu(0)/3$. To compute the precise value of this contribution for arbitrary disorder strength, as well as its evolution with temperature, we resort to the numerical computation.

In the top row of Figs. 3(a)–3(d), we plot the total density of states for the same numerical parameters $u = -0.035$ and $\lambda_1 = \lambda_2 = -0.17$. The DOS is determined self-consistently for varying Γ/Δ_2 and fixed $\nu_2/\nu_1 = 0.15$, based on the experimental results on 4Hb-TaS$_2$ in Ref. [11]. As Γ increases, states begin to fill the gap. When $\Gamma \gg \Delta_2$ and Eq. (8) holds, the density of states of band 2 near $\omega = 0$ is almost constant, as in a metal. We note that this limit is robust, as it yields
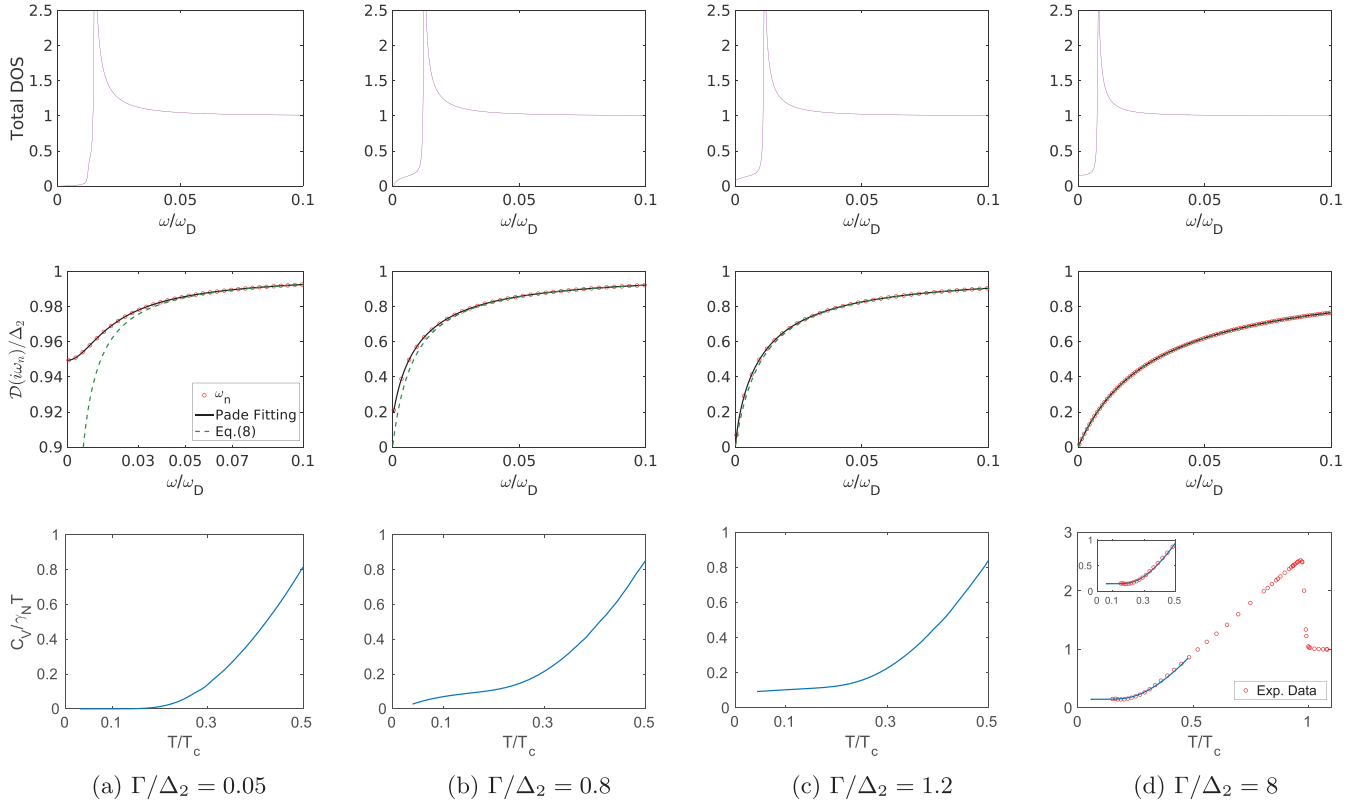
(a) $\Gamma/\Delta_2 = 0.05$ (b) $\Gamma/\Delta_2 = 0.8$ (c) $\Gamma/\Delta_2 = 1.2$ (d) $\Gamma/\Delta_2 = 8$

FIG. 3. The first two rows present the normalized tunneling density of states $\nu(\omega)/\nu_0$ for $u = -0.035$, $\lambda_1 = \lambda_2 = -0.17$, where ν_0 is the density of states at the absence of superconductivity, and the Matsubara-frequency dependent gap function $\mathcal{D}(i\omega_n)/\Delta_2$. The gap function in the middle row compared with the results from the Padé approximation used for the analytical continuation [31] and the asymptotic form at large Matsubara frequency given by Eq. (8). Clearly, the asymptotic form captures the entire frequency dependence of the gap in the limit of large Γ. The last row shows the corresponding heat capacity normalized by the normal state value $C_V/\gamma_N T$ as a function of T/T_c (note that T_c depends on Γ). The columns correspond to different values of the pair-breaking rate normalized by the value of the second gap Γ/Δ_2, which is determined self-consistently. Note that the largest value of Γ/Δ_2 is compared with the experimental data for the specific heat of $4Hb$-TaS$_2$ from Ref. [11].

nearly identical results for any larger Γ value. Thus, the tunneling density of states is expected to resemble that of a fully gapped and relatively clean superconductor, but simply shifted by a constant. In particular, the coherence peak remains sharp, in contrast to the case of gapless superconductivity in single-band systems, where the coherence peak is suppressed in the gapless regime [28]. In the middle row of Figs. 3(a)–3(d), we plot the corresponding gap function Eq. (10) versus Matsubara frequency. The gap is compared with the Padé approximation [31] (still in Matsubara space) and the asymptotic form, Eq. (8). These plots demonstrate that the asymptotic form of the gap is a good approximation in the limit of strong disorder.

Finally, we turn to the computation of the heat capacity $C_V/T = -\frac{\partial^2 F}{\partial T^2}$, where $F = k_B T \int_0^\infty \ln[1 - \exp(-\beta\omega)]\nu(\omega)d\omega$ is the free energy with Boltzmann's constant k_B and $\beta = (k_B T)^{-1}$. Note that if Δ is only weakly dependent on the temperature, one can estimate the heat capacity by the following expression [32]:

$$C_V \sim \frac{1}{T}\int_0^\infty \omega^2 \left(-\frac{\partial f(\omega)}{\partial \omega}\right)\nu(\omega)d\omega, \quad T \to 0, \qquad (12)$$

where $f(\omega) = (1 + e^{\omega/k_B T})^{-1}$ is the Fermi-Dirac distribution function. At low temperatures ($T \lesssim T_c/2$), the results from

this expression coincide with the numerical calculations. In the bottom row of Figs. 3(a)–3(d), we plot the corresponding heat capacity normalized by the normal state contribution. Note that the numerical calculation of the gap and the analytic continuation become unstable close to the transition point. Therefore we plot the computed heat capacity only up to $T = T_c/2$. In column (d), we compare the results in the strong disorder regime with the experimental data from Ref. [11]. Excellent agreement is found for the low-temperature behavior. This demonstrates that the experimental observation is consistent with our toy model's predictions.

III. BAND STRUCTURE OF $4Hb$-TaS$_2$

After having established a simple toy model that demonstrates robust gapless superconductivity over a wide parameter range, we now discuss its relevance to $4Hb$-TaS$_2$. Our first step is to construct a realistic tight-binding model from density-functional theory (DFT). We obtain a 12-band tight-binding model using DFT and maximally localized Wannier functions using the VASP code and the projector-augmented-wave approach [33,34]. The exchange-correlation functional was approximated using the Perdew-Burke-Ernzerhof potentials, which employ the generalized gradient approximation
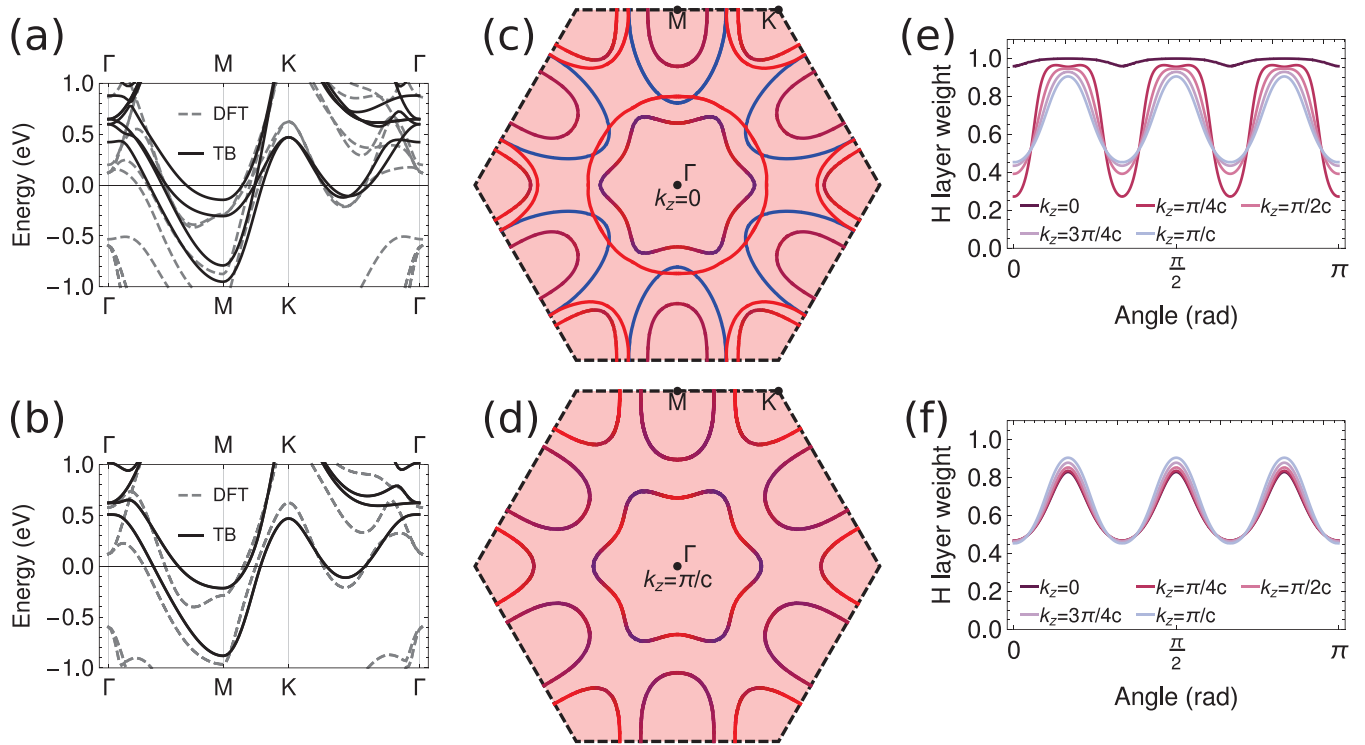
FIG. 4. (a),(b) Comparison of DFT (black, solid) and tight-binding (TB; gray, dashed) band structures for (a) $k_z = 0$ and (b) $k_z = \pm\pi/c$. The twofold degeneracy is clear for $k_z = \pm\pi/c$ and it is correctly captured by the tight-binding model. (c),(d) Fermi surfaces for $k_z = 0$ and $k_z = \pm\pi/c$. They consist of pairs of pockets centered at the high-symmetry points of the Brillouin zone, Γ, M, and K. These pairs become degenerate at $k_z = \pm\pi/c$ due to the screw symmetry of the crystal. The Fermi pockets are colored red (blue) according to their H-layer (T-layer) spectral weight. Therefore, purple means more strongly hybridized pockets. (e),(f) Layer weights along outer (up) and inner (down) Gamma pockets. Outer pocket becomes strongly hybridized away from $k_z = 0$.

[35]. As the unit cell is highly extended in the stacking direction, a Γ-centered k-points grid of $11 \times 11 \times 2$ was used along with a plane-wave cutoff of 470 eV. Structural parameters were taken from experiments [19].

The tight-binding model parameters were obtained by constructing maximally localized Wannier functions using the WANNIER90 package [36,37]. It consists of 12 Ta orbitals, 3 per Ta atom per layer. The shape of these orbitals is different for atoms in the T layer and in the H layer (see Appendix A) with the T layer having standard t_{2g} orbitals and the H layer having unconventional orbitals. The tight-binding parameters used here to reproduce the features of the Fermi surface and the low-energy band structure contain only on-site terms, nearest-neighbor hopping, and a single interlayer hopping term. They can be found in Table I in Appendix A.

The crystal structure of 4Hb-TaS$_2$ is invariant under a 6_3 screw operation, which is equivalent to a 60° rotation around the z axis, followed by a half-unit cell translation along the same axis. The structure is also invariant under a 120° rotation around $\hat{\mathbf{z}}$, and the consecutive application of this rotation with the 6_3 screw gives the 2_1 screw operation, which we denote as s. s is a 180° rotation followed by a half-unit cell translation.

The Bloch wave-function representation of the nonsymmorphic screw symmetry s of the 4Hb compound squares to minus one, $s^2 = -1$, at $k_z = \pm\pi/c$. Due to this nonsymmorphic symmetry, the band structure becomes doubly degenerate (fourfold including Kramers degeneracy) at all k points on the $k_z = \pm\pi/c$. This can be seen by noting the relationships

between the screw symmetry s, the mirror plane parallel to the H planes (m_{001}), and the inversion (i) with inversion centers at the T-layer Ta atoms. Because $s = mi$ and $m^2 = i^2 = 1$, one would expect that $s^2 = 1$. But, as discussed above, $s^2 = -1$ at $k_z = \pm\pi/c$. This apparent contradiction is resolved by enforcing a twofold degeneracy throughout the $k_z = \pm\pi/c$ plane, with these degenerate wave functions being related by s [38,39].

The resulting DFT band structures at $k_z = 0$ and $k_z = \pm\pi/c$ are shown in Figs. 4(a) and 4(b), along with the tight-binding dispersions. The latter reproduces the correct number of distinct Fermi surfaces, shown in Figs. 4(c) and 4(d), which consist of pairs of split inner and outer pockets at Γ, M, and K—except at the $k_z = \pm\pi/c$ planes, where the inner and outer pockets become degenerate.

The Fermi pockets in Figs. 4(c) and 4(d) are colored according to their spectral weights, with red (blue) denoting spectral weight due to states from an H (T) layer. Figures 4(e) and 4(f) show the spectral weight along the outer and inner Γ pockets. For $k_z = 0$, while all inner pockets have a strong mixed-layer character (as indicated by their purple color), the outer pockets are made out of states from nearly a single layer only. In particular, the outer pockets at Γ and K have a predominant H-layer character, whereas the outer pocket at M has a dominant T-layer character. Thus, the H-T interlayer hybridization is different for each of the Fermi pockets that form a pair of pockets centered at the same high-symmetry point of the Brillouin zone. As k_z increases towards

$k_z = \pm\pi/c$, the interlayer hybridization becomes comparable for the pockets that form a pair.

This behavior can be understood from the fact that the H-T hybridization between crossing bands depends on their mirror eigenvalues. There is a mirror plane on each H layer, and Bloch states on the $k_z = 0$ plane have a mirror eigenvalue of either $+1$ or -1. Symmetry dictates that the orbitals on the H layers induce bands with $+1$ mirror eigenvalues only, whereas the orbitals on T layers induce equal numbers of $+1$ and -1 eigenvalue bands.

Hybridization between the $+$ and $-$ eigenvalue bands is forbidden on the $k_z = 0$ plane, since these k vectors do not break the mirror symmetry. As a result, the T layers that have -1 mirror eigenvalue can cross the H layers without hybridization on this plane.

IV. PAIR BREAKING DUE TO MAGNETIC FLUCTUATIONS ON THE T LAYERS

We now connect the band structure calculations with our two-band toy model. Motivated by the fact that the $2H$ polymorph is a superconductor, whereas the $1T$ polymorph is a Mott insulator, we focus on the Fermi pockets of the $4Hb$ polymorph with dominant H-layer character, i.e., the pairs of pockets centered at Γ and K in Fig. 4(c). We further neglect large-momentum pairing interactions, and therefore consider each pair of pockets as an independent two-band model. In other words, the two bands in our toy model correspond to the inner and outer Fermi pockets centered at the same high-symmetry point of the Brillouin zone (Γ or K).

Our working hypothesis is that superconductivity would emerge in these two pockets intrinsically, driven by the same intrapocket pairing interaction that makes the $2H$ polymorph a superconductor. The key difference in the $4Hb$ compound is that these bands hybridize with the T-layer states, as we discussed above. Now, the $1T$ polymorph is a Mott insulator, presumably with strongly fluctuating local moments that do not order magnetically. We assume that these local-moment fluctuations persist in the $4Hb$ compound, since it also undergoes a star-of-David CDW transition. These magnetic fluctuations on the T layer will then cause pair breaking in the superconducting H-layer pockets via the H-T interlayer hybridization. Because the hybridization is significantly different for the two pockets, particularly near $k_z = 0$, the pair-breaking effect is expected to be of very distinct magnitudes in each pocket.

A full description of the local moments in the T layer and of their coupling to the H-layer itinerant states is well beyond the scope of this work. To capture the pair-breaking effect caused by these magnetic fluctuating moments, we model them as dilute magnetic impurities. We then compute the single-particle lifetime in the pairs of Fermi pockets centered at Γ and K due to such impurities residing on the T layers, in order to verify that the pair-breaking potential is significantly different in the inner and outer pockets centered at each momentum.

We start from the bare Green's function in the *band basis*

$$G_0^j(i\omega, \boldsymbol{k}) = \frac{1}{-i\omega + (\varepsilon_{\boldsymbol{k},j} - \varepsilon_F)}, \qquad (13)$$

where $\varepsilon_{\boldsymbol{k},j}$ are the eigenvalues of the 12×12 tight-binding Hamiltonian (see Appendix A).

The single-particle scattering amplitude between the states $|\mathbf{k}\alpha\rangle$ and $|\mathbf{p}\beta\rangle$ in the *orbital basis* is given by

$$\widehat{\mathbf{V}}_{\alpha,\beta}(\mathbf{k},\mathbf{p}) = \sum_{l=1}^{N_{\mathrm{imp}}} V_l \mathrm{e}^{i(k-p)\cdot r_l} M_{\alpha,\beta}, \qquad (14)$$

where $\mathbf{k}$, $\mathbf{p}$ denote momenta states and α, β denote the orbitals (corresponding to the three d orbitals on the four layers). N_{imp} is the number of impurities, $\boldsymbol{r}_l$ are their positions, and V_l is the random pointlike disorder potential strength, which has zero mean and variance V^2. The matrix M encodes the orbital structure of the scattering process. Following our convention of T-H-T-H stacking, we model the impurities in the T layers by the matrix

$$M = \begin{pmatrix} \mathbb{1} & 0 & 0 & 0 \\ 0 & 0 & 0 & 0 \\ 0 & 0 & \mathbb{1} & 0 \\ 0 & 0 & 0 & 0 \end{pmatrix}, \qquad (15)$$

where $\mathbb{1}$ is a 3×3 identity matrix. For the purposes of computing the lifetime, which is only a proxy for the pair-breaking scattering rate, it is fine to consider such a nonmagnetic potential, since the tight-binding model is SU(2) symmetric.

We now rotate the scattering matrix M in Eq. (14) to the band basis, which results in a form factor $Q(\boldsymbol{k},\boldsymbol{p}) = U^\dagger(\mathbf{k})MU(\mathbf{p})$, where $U(\mathbf{k})$ is the unitary transformation matrix that takes the tight-binding Hamiltonian from the orbital basis to the band basis. Then the self-energy is given by

$$\Sigma(i\omega, \boldsymbol{k}) = \frac{n_{\mathrm{imp}}V^2}{\Omega_{BZ}} \int_{BZ} d^3 p \, Q(\boldsymbol{k},\boldsymbol{p})G_0(i\omega,\boldsymbol{p})Q(\boldsymbol{p},\boldsymbol{k}), \quad (16)$$

where Ω_{BZ} is the volume of the Brillouin zone, n_{imp} is the impurity density, and the integration is over the entire Brillouin zone [40]. The inverse lifetime can then be calculated via

$$\Gamma(\boldsymbol{k}) = \mathrm{Im}\left[\Sigma(i\omega \to 0^+, \boldsymbol{k}) - \Sigma(i\omega \to 0^-, \boldsymbol{k})\right]. \qquad (17)$$

The inverse lifetime Γ is plotted in Fig. 5 for three different k_z planes: $k_z = 0$, $k_z = \pm\pi/2c$, and $k_z = \pm\pi/c$. In particular, for each column, we show the inverse lifetime on the inner (green) and outer (violet) Fermi pockets centered at the Γ and K points (i.e., the Fermi pockets with predominant H character). We find that, at $k_z = 0$, the inverse lifetimes on the inner Fermi pockets are orders of magnitude larger than those on the outer pockets. However, as we move away from the $k_z = 0$ plane, the inverse lifetimes on the outer pockets grow rapidly and become nearly equal to those on the inner pockets. We also note that the scattering rate on the K pockets is consistently smaller than that of Γ pockets.

Based on these results, and using the inverse lifetime as a proxy for the pair-breaking scattering rate, we conclude that the scattering rate in $4Hb$-TaS$_2$ depends strongly on the Fermi surface. This qualitatively justifies the toy model studied in Sec. II. The difference is greatest when scattering involving the $k_z = 0$ states provides the dominant pair-breaking channel.
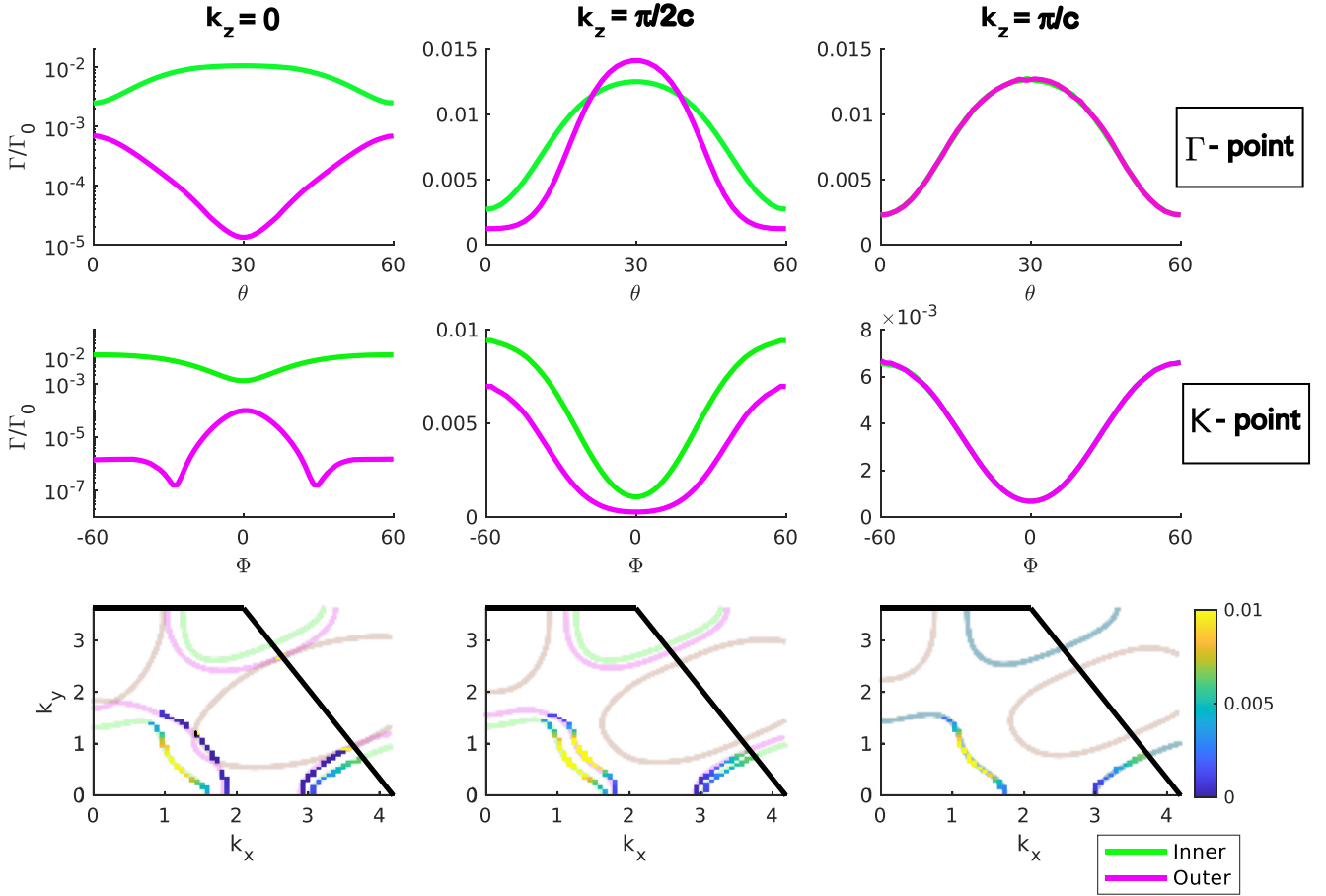
FIG. 5. The inverse lifetime Γ due to scattering by impurities, Eq. (17), normalized by $\Gamma_0 = n_{\text{imp}} V^2/\Omega_{BZ} W$, where Ω_{BZ} is the volume of the Brillouin zone and $W \sim 1$ [eV] is comparable to the typical bandwidth. This quantity is a proxy for the pair-breaking scattering rate. The inverse lifetime is presented for different k_z values for the inner (green) and outer (violet) pockets centered at the Γ (upper panel) and K (middle panel) points. The angle is measured with respect to $k_y = 0$, where θ starts at $(0, 0)$ counterclockwise, and Φ at $(4\pi/3, 0)$ clockwise. At $k_z = 0$, the inverse lifetime on the outer pocket is orders of magnitude smaller than that in the inner one (note that in this case the plot is logarithmic in the y axis). However, it grows rapidly and becomes equal to the latter as the zone boundary is approached. The lower panel shows the same inverse lifetime, overlaid on the corresponding Fermi pockets at the right corner of the Brillouin zone (marked by thick black lines). Here we can also observe a considerable difference between the K pockets and the Γ pockets.

V. DISCUSSION

In this paper we proposed a simple scenario for the superconducting ground state of $4Hb$-TaS$_2$. In particular, we showed that the puzzling T-linear specific heat that is observed experimentally at low temperatures is naturally explained when the pair-breaking scattering rate varies significantly between the different Fermi pockets of a two-band superconductor. In this situation, the well-known gapless superconducting state predicted by Abrikosov and Gor'kov [26] is stabilized over a wide range of parameters. The presence of both a fully gapped superconducting pocket and a gapless superconducting pocket ensures the existence of sharp coherent peaks at the density of states and of a sharp specific heat jump at T_c.

To show the relevance of this toy model to $4Hb$-TaS$_2$, we derived a tight-binding model for this compound from DFT. We find that the DFT band structure is well captured within a nearest-neighbor tight-binding approximation including only one (diagonal) interlayer hopping term. In addition, the

special screw symmetry of this compound forces a degenerate doublet of Fermi pockets at the zone top and bottom, which are otherwise nondegenerate and form "inner" and "outer" Fermi pockets surrounding the Γ, K, and M points.

We then employed this tight-binding model to estimate the expected pair-breaking scattering rates on the different Fermi sheets with predominant H-layer character, caused by magnetic fluctuations residing on the strongly correlated T layers. We found the rates can be notably different when comparing the inner vs outer Fermi surfaces. In particular, near the $k_z = 0$ plane, the inner pockets experience a scattering rate that is more than two orders of magnitude larger than that experienced by the outer pockets. Additionally, we also observe a considerable difference between the scattering rate on Fermi pockets surrounding K and those surrounding Γ throughout the entire Brillouin zone. We note that pocket-dependent pair-breaking and multigap superconductivity were recently observed in the related compound $2H$-NbSe$_2$ [10]. Moreover, recent magnetotransport measurements performed on $4Hb$-TaS$_2$ reveal a large

variability of the mobility of carriers on the different Fermi pockets [41].

It is important to note that our tight-binding model neglects the effects of spin-orbit coupling and the CDW phases in both T and H layers. While we checked that the influence of the spin-orbit coupling on the band structure is weak compared to the impact of the interlayer coupling, the CDW phases may have a more important effect. For example, it is possible that the H-T hybridization is significantly modified. Nevertheless, the conclusion that a Fermi-surface dependent scattering rate leads to robust gapless superconductivity is more general, and may even apply to other superconductors exhibiting anomalous specific heat behavior [22].

In this paper, we assumed that the magnetic disorder is static. However, it is interesting to consider the implications of dynamic fluctuations, in which the inner Fermi pockets may Kondo screen them. We note that Kondo screening between the T and H layers of TaSe$_2$ was recently reported [42]. Such a screening may also occur inside the superconducting state, as the inner Fermi surfaces are gapless [43]. In fact, it is possible that the Josephson coupling to the outer Fermi pockets competes (weakly) with the Kondo screening and causes a partial unscreening of the magnetic moments. We thus raise the question whether this may be a possible source for the enhanced muon relaxation observed below T_c, which would then be unrelated to chiral superconductivity.

We also note that such a Kondo-screened state is not expected to leave signatures in transport because the gapped superconducting Fermi pockets shunt the gapless ones. To observe these effects, we propose the use of local probes with scanning capabilities such as scanning SQUID, scanning tunneling microscopy, and compressibility sensors. When the Kondo temperature is low, it may be possible to unscreen the magnetic moments in a magnetic field and observe an anomalous magnetic response even above the superconducting transition temperature.

APPENDIX A: DETAILS OF THE TIGHT-BINDING MODEL

Our tight-binding Hamiltonian has three orbitals per Ta atom, as presented in Fig. 6, where we show the maximally localized Wannier orbitals used to construct it.

The Wannier function calculations are initialized by using random projections; in other words, the shapes and
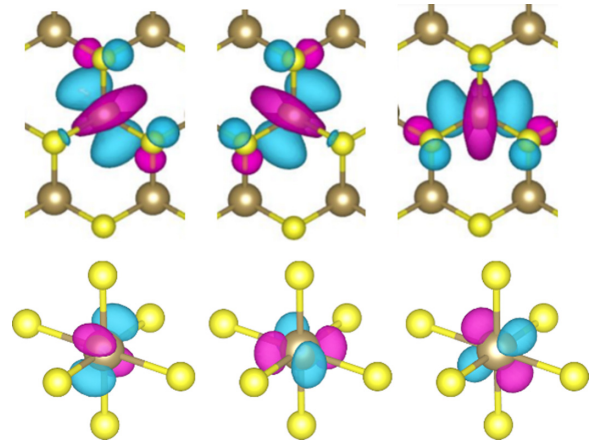

FIG. 6. Maximally localized Wannier orbitals for H layer (upper panel) and T layer (lower panel).

symmetries of these orbitals are not imposed manually and are rather an outcome of the calculation. Even though the site symmetry of the Ta sites on the T layer ($\bar{3}m$) is not cubic, the deviation from the cubic symmetry is not strong in the crystal field, and the resulting Wannier orbitals are very similar to the d_{xy}, d_{xz}, and d_{yz} cubic harmonics with Cartesian axes chosen parallel to the Ta-S bonds (Fig. 6, bottom panel).

For the H layer (upper panel), all three Wannier orbitals have shapes similar to the $d_{3z^2-r^2}$ orbital, but they are oriented in-plane and towards a neighboring pair of Ta atoms. The shape of these orbitals is a result of the local crystal field. The site symmetry of the Ta site on the H layers is $\bar{6}m2$. The trigonal prismatic crystal field splits the otherwise fivefold degenerate d levels into a doublet and a singlet, where the energy splitting of the lower doublet and the singlet is $\sim$100 meV in TaS$_2$. For z axis chosen normal to the H layer, the singlet, which transforms as the A_1' irrep, has $d_{3z^2-r^2}$ character. Similarly, the lower doublet, which transforms at the E' irrep, has $(d_{xy}, d_{x^2-y^2})$ character. The following superpositions of these three cubic harmonic orbitals give three orbitals, similar to those in the upper panel of Fig. 6, which transform to each other under 120° rotations:

$$d_1 = -\sqrt{\frac{1}{3}}d_{3z^2-r^2} + \sqrt{\frac{2}{3}}d_{x^2-y^2},$$

$$d_2 = -\sqrt{\frac{1}{3}}d_{3z^2-r^2} - \sqrt{\frac{1}{2}}d_{xy} - \sqrt{\frac{1}{6}}d_{x^2-y^2}, \quad \text{(A1)}$$

$$d_3 = -\sqrt{\frac{1}{3}}d_{3z^2-r^2} + \sqrt{\frac{1}{2}}d_{xy} - \sqrt{\frac{1}{6}}d_{x^2-y^2}.$$

These orbitals are orthonormal [44]. The Wannier functions do not have exactly the same form as in Eq. (A1), for they also include the hybridization between different orbitals and atoms. Also, note that the $d_{3z^2-r^2}$ orbital oriented along the x direction, which we call $d_{3x^2-r^2}$, can be written as

$$d_{3x^2-r^2} = -\frac{1}{2}d_{3z^2-r^2} + \frac{\sqrt{3}}{2}d_{x^2-y^2}. \quad \text{(A2)}$$

Thus, the orbital character of d_1 is very similar to $d_{3x^2-r^3}$, except for the loss of continuous rotational symmetry around the x axis, which does not exist in the crystal.

In summary, we find that on every layer of TaS$_2$, there are three different atom-centered Wannier orbitals that need to be included in the tight-binding model. This leads to a 12×12 tight-binding Hamiltonian. We include on-site off-diagonal terms on the H layers, and select in-plane nearest-neighbor hopping terms, in addition to one out-of-plane term. The layers are specified in stacking order T-H-T-H. The structure of the matrix is

$$
\widehat{\mathbf{H}} = \begin{pmatrix}
\xi_{1,1} & 0 & 0 & \xi_{1,4} & 0 & 0 & 0 & 0 & 0 & \xi_{1,10} & 0 & 0 \\
0 & \xi_{2,2} & 0 & 0 & \xi_{2,5} & 0 & 0 & 0 & 0 & 0 & \xi_{2,11} & 0 \\
0 & 0 & \xi_{3,3} & 0 & 0 & \xi_{3,6} & 0 & 0 & 0 & 0 & 0 & \xi_{3,12} \\
\xi_{1,4}^* & 0 & 0 & \xi_{4,4} & \xi_{4,5} & \xi_{4,6} & \xi_{4,7} & 0 & 0 & 0 & 0 & 0 \\
0 & \xi_{2,5}^* & 0 & \xi_{4,5}^* & \xi_{5,5} & \xi_{5,6} & 0 & \xi_{5,8} & 0 & 0 & 0 & 0 \\
0 & 0 & \xi_{3,6}^* & \xi_{4,6}^* & \xi_{5,6}^* & \xi_{6,6} & 0 & 0 & \xi_{6,9} & 0 & 0 & 0 \\
0 & 0 & 0 & \xi_{4,7}^* & 0 & 0 & \xi_{7,7} & 0 & 0 & \xi_{7,10} & 0 & 0 \\
0 & 0 & 0 & 0 & \xi_{5,8}^* & 0 & 0 & \xi_{8,8} & 0 & 0 & \xi_{8,11} & 0 \\
0 & 0 & 0 & 0 & 0 & \xi_{6,9}^* & 0 & 0 & \xi_{9,9} & 0 & 0 & \xi_{9,12} \\
\xi_{1,10}^* & 0 & 0 & 0 & 0 & 0 & \xi_{7,10}^* & 0 & 0 & \xi_{10,10} & \xi_{10,11} & \xi_{10,12} \\
0 & \xi_{2,11}^* & 0 & 0 & 0 & 0 & 0 & \xi_{8,11}^* & 0 & \xi_{10,11}^* & \xi_{11,11} & \xi_{11,12} \\
0 & 0 & \xi_{3,12}^* & 0 & 0 & 0 & 0 & 0 & \xi_{9,12}^* & \xi_{10,12}^* & \xi_{11,12}^* & \xi_{12,12}
\end{pmatrix}. \tag{A3}
$$

The matrix elements are given by

$$\xi_{1,1} = \varepsilon_H - 2t_1 \cos(\boldsymbol{k} \cdot \boldsymbol{x}_3) + 2t_2[\cos(\boldsymbol{k} \cdot \boldsymbol{x}_1) + \cos(\boldsymbol{k} \cdot \boldsymbol{x}_2)],$$

$$\xi_{1,4} = -t_z\{i \sin[\boldsymbol{k} \cdot (\boldsymbol{c}_1 + \boldsymbol{x}_1)] + i \sin[\boldsymbol{k} \cdot (\boldsymbol{c}_1 - \boldsymbol{x}_2)] + \cos[\boldsymbol{k} \cdot (\boldsymbol{c}_1 + \boldsymbol{x}_1)] + \cos[\boldsymbol{k} \cdot (\boldsymbol{c}_1 - \boldsymbol{x}_2)]\},$$

$$\xi_{1,10} = -t_z\{-i \sin[\boldsymbol{k} \cdot (\boldsymbol{c}_1 + \boldsymbol{x}_1)] - i \sin[\boldsymbol{k} \cdot (\boldsymbol{c}_1 - \boldsymbol{x}_2)] + \cos[\boldsymbol{k} \cdot (\boldsymbol{c}_1 + \boldsymbol{x}_1)] + \cos[\boldsymbol{k} \cdot (\boldsymbol{c}_1 - \boldsymbol{x}_2)]\},$$

$$\xi_{2,2} = \varepsilon_H - 2t_1 \cos(\boldsymbol{k} \cdot \boldsymbol{x}_1) + 2t_2[\cos(\boldsymbol{k} \cdot \boldsymbol{x}_2) + \cos(\boldsymbol{k} \cdot \boldsymbol{x}_3)],$$

$$\xi_{2,5} = t_z\{i \sin[\boldsymbol{k} \cdot (\boldsymbol{c}_1 + \boldsymbol{x}_2)] + i \sin[\boldsymbol{k} \cdot (\boldsymbol{c}_1 + \boldsymbol{x}_3)] + \cos[\boldsymbol{k} \cdot (\boldsymbol{c}_1 + \boldsymbol{x}_2)] + \cos[\boldsymbol{k} \cdot (\boldsymbol{c}_1 + \boldsymbol{x}_3)]\},$$

$$\xi_{2,11} = t_z\{-i \sin[\boldsymbol{k} \cdot (\boldsymbol{c}_1 + \boldsymbol{x}_2)] - i \sin[\boldsymbol{k} \cdot (\boldsymbol{c}_1 + \boldsymbol{x}_3)] + \cos[\boldsymbol{k} \cdot (\boldsymbol{c}_1 + \boldsymbol{x}_2)] + \cos[\boldsymbol{k} \cdot (\boldsymbol{c}_1 + \boldsymbol{x}_3)]\},$$

$$\xi_{3,3} = \varepsilon_H - 2t_1 \cos(\boldsymbol{k} \cdot \boldsymbol{x}_2) + 2t_2[\cos(\boldsymbol{k} \cdot \boldsymbol{x}_1) + \cos(\boldsymbol{k} \cdot \boldsymbol{x}_3)],$$

$$\xi_{3,6} = -t_z\{i \sin[\boldsymbol{k} \cdot (\boldsymbol{c}_1 - \boldsymbol{x}_1)] + i \sin[\boldsymbol{k} \cdot (\boldsymbol{c}_1 - \boldsymbol{x}_3)] + \cos[\boldsymbol{k} \cdot (\boldsymbol{c}_1 - \boldsymbol{x}_1)] + \cos[\boldsymbol{k} \cdot (\boldsymbol{c}_1 - \boldsymbol{x}_3)]\},$$

$$\xi_{3,12} = -t_z\{-i \sin[\boldsymbol{k} \cdot (\boldsymbol{c}_1 - \boldsymbol{x}_1)] - i \sin[\boldsymbol{k} \cdot (\boldsymbol{c}_1 - \boldsymbol{x}_3)] + \cos[\boldsymbol{k} \cdot (\boldsymbol{c}_1 - \boldsymbol{x}_1)] + \cos[\boldsymbol{k} \cdot (\boldsymbol{c}_1 - \boldsymbol{x}_3)]\},$$

$$\xi_{4,4} = \varepsilon_T - 2t_3 \cos(\boldsymbol{k} \cdot \boldsymbol{x}_3) + 2t_4[\cos(\boldsymbol{k} \cdot \boldsymbol{x}_1) + \cos(\boldsymbol{k} \cdot \boldsymbol{x}_2)],$$

$$\begin{aligned}\xi_{4,5} = {}& t_o + t_6[-i \sin(\boldsymbol{k} \cdot \boldsymbol{x}_1) + i \sin(\boldsymbol{k} \cdot \boldsymbol{x}_3) + \cos(\boldsymbol{k} \cdot \boldsymbol{x}_1) + \cos(\boldsymbol{k} \cdot \boldsymbol{x}_3)] + t_7[i \sin(\boldsymbol{k} \cdot \boldsymbol{x}_2) - \cos(\boldsymbol{k} \cdot \boldsymbol{x}_2)] \\ & + t_8[i \sin(\boldsymbol{k} \cdot \boldsymbol{x}_2) + \cos(\boldsymbol{k} \cdot \boldsymbol{x}_2)] - t_5[i \sin(\boldsymbol{k} \cdot \boldsymbol{x}_1) - i \sin(\boldsymbol{k} \cdot \boldsymbol{x}_3) + \cos(\boldsymbol{k} \cdot \boldsymbol{x}_1) + \cos(\boldsymbol{k} \cdot \boldsymbol{x}_3)],\end{aligned}$$

$$\begin{aligned}\xi_{4,6} = {}& t_o + t_6[i \sin(\boldsymbol{k} \cdot \boldsymbol{x}_2) - i \sin(\boldsymbol{k} \cdot \boldsymbol{x}_3) + \cos(\boldsymbol{k} \cdot \boldsymbol{x}_2) + \cos(\boldsymbol{k} \cdot \boldsymbol{x}_3)] - t_7[i \sin(\boldsymbol{k} \cdot \boldsymbol{x}_1) + \cos(\boldsymbol{k} \cdot \boldsymbol{x}_1)] \\ & + t_8[-i \sin(\boldsymbol{k} \cdot \boldsymbol{x}_1) + \cos(\boldsymbol{k} \cdot \boldsymbol{x}_1)] - t_5[-i \sin(\boldsymbol{k} \cdot \boldsymbol{x}_2) + i \sin(\boldsymbol{k} \cdot \boldsymbol{x}_3) + \cos(\boldsymbol{k} \cdot \boldsymbol{x}_2) + \cos(\boldsymbol{k} \cdot \boldsymbol{x}_3)],\end{aligned}$$

$$\xi_{4,7} = -t_z\{i \sin[\boldsymbol{k} \cdot (\boldsymbol{c}_1 - \boldsymbol{x}_1)] + i \sin[\boldsymbol{k} \cdot (\boldsymbol{c}_1 + \boldsymbol{x}_2)] + \cos[\boldsymbol{k} \cdot (\boldsymbol{c}_1 - \boldsymbol{x}_1)] + \cos[\boldsymbol{k} \cdot (\boldsymbol{c}_1 + \boldsymbol{x}_2)]\},$$

$$\xi_{5,5} = \varepsilon_T - 2t_3 \cos(\boldsymbol{k} \cdot \boldsymbol{x}_1) + 2t_4[\cos(\boldsymbol{k} \cdot \boldsymbol{x}_2) + \cos(\boldsymbol{k} \cdot \boldsymbol{x}_3)],$$

$$\begin{aligned}\xi_{5,6} = {}& t_o + t_6[-i \sin(\boldsymbol{k} \cdot \boldsymbol{x}_1) - i \sin(\boldsymbol{k} \cdot \boldsymbol{x}_2) + \cos(\boldsymbol{k} \cdot \boldsymbol{x}_1) + \cos(\boldsymbol{k} \cdot \boldsymbol{x}_2)] - t_7[i \sin(\boldsymbol{k} \cdot \boldsymbol{x}_3) + \cos(\boldsymbol{k} \cdot \boldsymbol{x}_3)] \\ & + t_8[-i \sin(\boldsymbol{k} \cdot \boldsymbol{x}_3) + \cos(\boldsymbol{k} \cdot \boldsymbol{x}_3)] - t_5[i \sin(\boldsymbol{k} \cdot \boldsymbol{x}_1) + \sin(\boldsymbol{k} \cdot \boldsymbol{x}_2) + \cos(\boldsymbol{k} \cdot \boldsymbol{x}_1) + \cos(\boldsymbol{k} \cdot \boldsymbol{x}_2)],\end{aligned}$$

$$\xi_{5,8} = t_z\{i \sin[\boldsymbol{k} \cdot (\boldsymbol{c}_1 - \boldsymbol{x}_2)] + i \sin[\boldsymbol{k} \cdot (\boldsymbol{c}_1 - \boldsymbol{x}_3)] + \cos[\boldsymbol{k} \cdot (\boldsymbol{c}_1 - \boldsymbol{x}_2)] + \cos[\boldsymbol{k} \cdot (\boldsymbol{c}_1 - \boldsymbol{x}_3)]\},$$

$$\xi_{6,6} = \varepsilon_T - 2t_3 \cos(\boldsymbol{k} \cdot \boldsymbol{x}_2) + 2t_4[\cos(\boldsymbol{k} \cdot \boldsymbol{x}_1) + \cos(\boldsymbol{k} \cdot \boldsymbol{x}_3)],$$

$$\xi_{6,9} = -t_z\{i \sin[\boldsymbol{k} \cdot (\boldsymbol{c}_1 + \boldsymbol{x}_1)] + i \sin[\boldsymbol{k} \cdot (\boldsymbol{c}_1 + \boldsymbol{x}_3)] + \cos[\boldsymbol{k} \cdot (\boldsymbol{c}_1 + \boldsymbol{x}_1)] + \cos[\boldsymbol{k} \cdot (\boldsymbol{c}_1 + \boldsymbol{x}_3)]\},$$

$$\xi_{7,7} = \varepsilon_H - 2t_1 \cos(\boldsymbol{k} \cdot \boldsymbol{x}_3) + 2t_2[\cos(\boldsymbol{k} \cdot \boldsymbol{x}_1) + \cos(\boldsymbol{k} \cdot \boldsymbol{x}_2)],$$

$$\xi_{7,10} = -t_z\{i \sin[\boldsymbol{k} \cdot (\boldsymbol{c}_1 - \boldsymbol{x}_1)] + i \sin[\boldsymbol{k} \cdot (\boldsymbol{c}_1 + \boldsymbol{x}_2)] + \cos[\boldsymbol{k} \cdot (\boldsymbol{c}_1 - \boldsymbol{x}_1)] + \cos[\boldsymbol{k} \cdot (\boldsymbol{c}_1 + \boldsymbol{x}_2)]\},$$

$$\xi_{8,8} = \varepsilon_H - 2t_1 \cos(\boldsymbol{k} \cdot \boldsymbol{x}_1) + 2t_2[\cos(\boldsymbol{k} \cdot \boldsymbol{x}_2) + \cos(\boldsymbol{k} \cdot \boldsymbol{x}_3)],$$

$$\xi_{8,11} = t_z\{i \sin[\boldsymbol{k} \cdot (\boldsymbol{c}_1 - \boldsymbol{x}_2)] + i \sin[\boldsymbol{k} \cdot (\boldsymbol{c}_1 - \boldsymbol{x}_3)]) + \cos[\boldsymbol{k} \cdot (\boldsymbol{c}_1 - \boldsymbol{x}_2)] + \cos[\boldsymbol{k} \cdot (\boldsymbol{c}_1 - \boldsymbol{x}_3)]\},$$

$$\xi_{9,9} = \varepsilon_H - 2t_1 \cos(\boldsymbol{k} \cdot \boldsymbol{x}_2) + 2t_2[\cos(\boldsymbol{k} \cdot \boldsymbol{x}_1) + \cos(\boldsymbol{k} \cdot \boldsymbol{x}_3)],$$

$$\xi_{9,12} = -t_z\{i \sin[\boldsymbol{k} \cdot (\boldsymbol{c}_1 + \boldsymbol{x}_1)] + i \sin[\boldsymbol{k} \cdot (\boldsymbol{c}_1 + \boldsymbol{x}_3)] + \cos[\boldsymbol{k} \cdot (\boldsymbol{c}_1 + \boldsymbol{x}_1)] + \cos[\boldsymbol{k} \cdot (\boldsymbol{c}_1 + \boldsymbol{x}_3)\},$$

$$\xi_{10,10} = \varepsilon_T - 2t_3 \cos(\boldsymbol{k} \cdot \boldsymbol{x}_3) + 2t_4[\cos(\boldsymbol{k} \cdot \boldsymbol{x}_1) + \cos(\boldsymbol{k} \cdot \boldsymbol{x}_2)],$$

$$\xi_{10,11} = t_o + t_6[i\sin(\boldsymbol{k}\cdot\boldsymbol{x}_1) - i\sin(\boldsymbol{k}\cdot\boldsymbol{x}_3) + \cos(\boldsymbol{k}\cdot\boldsymbol{x}_1) + \cos(\boldsymbol{k}\cdot\boldsymbol{x}_3)] - t_7[i\sin(\boldsymbol{k}\cdot\boldsymbol{x}_2) + \cos(\boldsymbol{k}\cdot\boldsymbol{x}_2)]$$
$$+ t_8[-i\sin(\boldsymbol{k}\cdot\boldsymbol{x}_2) + \cos(\boldsymbol{k}\cdot\boldsymbol{x}_2)] - t_5[-i\sin(\boldsymbol{k}\cdot\boldsymbol{x}_1) + i\sin(\boldsymbol{k}\cdot\boldsymbol{x}_3) + \cos(\boldsymbol{k}\cdot\boldsymbol{x}_1) + \cos(\boldsymbol{k}\cdot\boldsymbol{x}_3)],$$
$$\xi_{10,12} = t_o + t_6[-i\sin(\boldsymbol{k}\cdot\boldsymbol{x}_2) + i\sin(\boldsymbol{k}\cdot\boldsymbol{x}_3) + \cos(\boldsymbol{k}\cdot\boldsymbol{x}_2) + \cos(\boldsymbol{k}\cdot\boldsymbol{x}_3)] + t_7[i\sin(\boldsymbol{k}\cdot\boldsymbol{x}_1) - \cos(\boldsymbol{k}\cdot\boldsymbol{x}_1)]$$
$$+ t_8[i\sin(\boldsymbol{k}\cdot\boldsymbol{x}_1) + \cos(\boldsymbol{k}\cdot\boldsymbol{x}_1)] - t_5[i\sin(\boldsymbol{k}\cdot\boldsymbol{x}_2) - i\sin(\boldsymbol{k}\cdot\boldsymbol{x}_3) + \cos(\boldsymbol{k}\cdot\boldsymbol{x}_2) + \cos(\boldsymbol{k}\cdot\boldsymbol{x}_3)],$$
$$\xi_{11,11} = \varepsilon_T - 2t_3\cos(\boldsymbol{k}\cdot\boldsymbol{x}_1) + 2t_4[\cos(\boldsymbol{k}\cdot\boldsymbol{x}_2) + \cos(\boldsymbol{k}\cdot\boldsymbol{x}_3)],$$
$$\xi_{11,12} = t_o + t_6[i\sin(\boldsymbol{k}\cdot\boldsymbol{x}_1) + i\sin(\boldsymbol{k}\cdot\boldsymbol{x}_2) + \cos(\boldsymbol{k}\cdot\boldsymbol{x}_1) + \cos(\boldsymbol{k}\cdot\boldsymbol{x}_2)] + t_7[i\sin(\boldsymbol{k}\cdot\boldsymbol{x}_3) - \cos(\boldsymbol{k}\cdot\boldsymbol{x}_3)]$$
$$+ t_8[i\sin(\boldsymbol{k}\cdot\boldsymbol{x}_3) + \cos(\boldsymbol{k}\cdot\boldsymbol{x}_3)] - t_5[-i\sin(\boldsymbol{k}\cdot\boldsymbol{x}_1) - i\sin(\boldsymbol{k}\cdot\boldsymbol{x}_2) + \cos(\boldsymbol{k}\cdot\boldsymbol{x}_1) + \cos(\boldsymbol{k}\cdot\boldsymbol{x}_2)],$$
$$\xi_{12,12} = \varepsilon_T - 2t_3\cos(\boldsymbol{k}\cdot\boldsymbol{x}_2) + 2t_4[\cos(\boldsymbol{k}\cdot\boldsymbol{x}_1) + \cos(\boldsymbol{k}\cdot\boldsymbol{x}_3)].$$

Here, $\boldsymbol{x}_{1,2,3}$ are the three nearest-neighbor vectors and $\boldsymbol{c}_1$ is the out-of-plane interlayer vector given by

$$\boldsymbol{x}_1 = a\widehat{\boldsymbol{x}}, \quad \boldsymbol{x}_2 = a\left(-\frac{1}{2}\widehat{\boldsymbol{x}} + \frac{\sqrt{3}}{2}\widehat{\boldsymbol{y}}\right),$$
$$\boldsymbol{x}_3 = a\left(\frac{1}{2}\widehat{\boldsymbol{x}} + \frac{\sqrt{3}}{2}\widehat{\boldsymbol{y}}\right), \quad \boldsymbol{c}_1 = \frac{c}{4}\widehat{\boldsymbol{z}}. \tag{A4}$$

The on-site terms and hopping parameters are given in Table I.

APPENDIX B: HEAT CAPACITY DATA AND NODAL SUPERCONDUCTIVITY

The working hypothesis of this paper is that the specific heat data is inconsistent with a nodal order parameter, even one that is lurking behind the T-linear contribution. In this Appendix we show that the specific heat is indeed inconsistent with such a nodal state, or at least that the nodal state is below the noise level of the experiment. To show this, we consider the temperature dependence of the derivative $\frac{d}{dT}(C_V/T)$ near $T = 0$. In the case of line nodes we expect

$$\text{line nodes}: \frac{d}{dT}\left(\frac{C_V}{T}\right) \sim \text{const}, \quad T \to 0,$$

TABLE I. Tight-binding parameters grouped by hopping matrix elements.

Onsite terms:	
ε_H	7.363
ε_T	6.577
t_o	-0.20
Nearest-neighbor terms:	
t_1	0.742
t_2	0.180
t_3	0.655
t_4	0.295
t_5	0.453
t_6	0.275
t_7	0.146
t_8	0.113
Interlayer term:	
t_z	0.081

while for point nodes

$$\text{point nodes}: \frac{d}{dT}\left(\frac{C_V}{T}\right) \sim T, \quad T \to 0.$$

In Fig. 7 we plot the numerical derivative $\frac{d}{dT}(\frac{C_V}{T})$ as a function of T on a log-log plot for the experimentally measured specific heat data. It is clear that in the temperature range below $T = 1$ K, the derivative is suppressed much faster than linear and is thus inconsistent with any kind of node. We thus conclude that C_V most likely decays exponentially to a constant, or at least, in the temperature range down to 0.3 K.
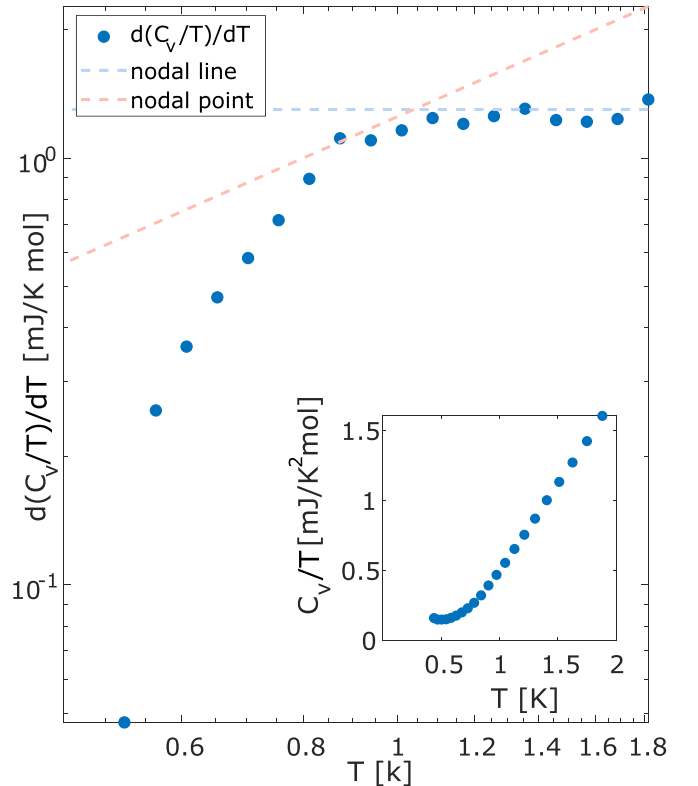

FIG. 7. The derivative $\frac{d}{dT}(\frac{C_V}{T})$ as a function of T on a log-log plot. The inset shows the raw data.

[1] B. Sipos, A. F. Kusmartseva, A. Akrap, H. Berger, L. Forró, and E. Tutiš, From Mott state to superconductivity in 1T-TaS$_2$, Nat. Mater. **7**, 960 (2008).

[2] D. K. Efetov, L. Wang, C. Handschin, K. B. Efetov, J. Shuang, R. Cava, T. Taniguchi, K. Watanabe, J. Hone, C. R. Dean *et al.*, Specular interband Andreev reflections at van der Waals interfaces between graphene and NbSe$_2$, Nat. Phys. **12**, 328 (2016).

[3] E. Navarro-Moratalla, J. O. Island, S. Manas-Valero, E. Pinilla-Cienfuegos, A. Castellanos-Gomez, J. Quereda, G. Rubio-Bollinger, L. Chirolli, J. A. Silva-Guillén, N. Agraït *et al.*, Enhanced superconductivity in atomically thin TaS$_2$, Nat. Commun. **7**, 11043 (2016).

[4] X. Xi, Z. Wang, W. Zhao, J.-H. Park, K. T. Law, H. Berger, L. Forró, J. Shan, and K. F. Mak, Ising pairing in superconducting NbSe$_2$ atomic layers, Nat. Phys. **12**, 139 (2016).

[5] M. M. Ugeda, A. J. Bradley, Y. Zhang, S. Onishi, Y. Chen, W. Ruan, C. Ojeda-Aristizabal, H. Ryu, M. T. Edmonds, H.-Z. Tsai *et al.*, Characterization of collective ground states in single-layer NbSe$_2$, Nat. Phys. **12**, 92 (2016).

[6] Y.-T. Hsu, A. Vaezi, M. H. Fischer, and E.-A. Kim, Topological superconductivity in monolayer transition metal dichalcogenides, Nat. Commun. **8**, 1 (2017).

[7] Y. Yang, S. Fang, V. Fatemi, J. Ruhman, E. Navarro-Moratalla, K. Watanabe, T. Taniguchi, E. Kaxiras, and P. Jarillo-Herrero, Enhanced superconductivity upon weakening of charge density wave transport in 2H-TaS$_2$ in the two-dimensional limit, Phys. Rev. B **98**, 035203 (2018).

[8] J. M. Lu, O. Zheliuk, I. Leermakers, N. F. Q. Yuan, U. Zeitler, K. T. Law, and J.T. Ye, Evidence for two-dimensional Ising superconductivity in gated MoS$_2$, Science **350**, 1353 (2015).

[9] V. Fatemi, S. Wu, Y. Cao, L. Bretheau, Q. D. Gibson, K. Watanabe, T. Taniguchi, R. J. Cava, and P. Jarillo-Herrero, Electrically tunable low-density superconductivity in a monolayer topological insulator, Science **362**, 926 (2018).

[10] T. Dvir, F. Massee, L. Attias, M. Khodas, M. Aprili, C. H. L. Quay, and H. Steinberg, Spectroscopy of bulk and few-layer superconducting NbSe$_2$ with van der Waals tunnel junctions, Nat. Commun. **9**, 598 (2018).

[11] A. Ribak, R. M. Skiff, M. Mograbi, P. K. Rout, M. H. Fischer, J. Ruhman, K. Chashka, Y. Dagan, and A. Kanigel, Chiral superconductivity in the alternate stacking compound 4Hb-TaS$_2$, Sci. Adv. **6**, eaax9480 (2020).

[12] A. Pustogow, Y. Luo, A. Chronister, Y.-S. Su, D. A. Sokolov, F. Jerzembeck, A. P. Mackenzie, C. W. Hicks, N. Kikugawa, S. Raghu *et al.*, Constraints on the superconducting order parameter in Sr$_2$RuO$_4$ from oxygen-17 nuclear magnetic resonance, Nature (London) **574**, 72 (2019).

[13] A. N. Petsch, M. Zhu, M. Enderle, Z. Q. Mao, Y. Maeno, I. I. Mazin, and S. M. Hayden, Reduction of the Spin Susceptibility in the Superconducting State of Sr$_2$RuO$_4$ Observed by Polarized Neutron Scattering, Phys. Rev. Lett. **125**, 217004 (2020).

[14] P. Fazekas and E. Tosatti, Charge carrier localization in pure and doped 1T-TaS$_2$, Physica B+C **99**, 183 (1980).

[15] K. T. Law and P. A. Lee, 1T-TaS$_2$ as a quantum spin liquid, Proc. Natl. Acad. Sci. USA **114**, 6996 (2017).

[16] A. Ribak, I. Silber, C. Baines, K. Chashka, Z. Salman, Y. Dagan, and A. Kanigel, Gapless excitations in the ground state of 1T-TaS$_2$, Phys. Rev. B **96**, 195131 (2017).

[17] H. Murayama, Y. Sato, T. Taniguchi, R. Kurihara, X. Z. Xing, W. Huang, S. Kasahara, Y. Kasahara, I. Kimchi, M. Yoshida, Y. Iwasa,Y. Mizukami, T. Shibauchi, M. Konczykowski, and Y. Matsuda, Effect of quenched disorder on the quantum spin liquid state of the triangular-lattice antiferromagnet 1T-TaS$_2$, Phys. Rev. Research **2**, 013099 (2020).

[18] Y. D. Wang, W. L. Yao, Z. M. Xin, T. T. Han, Z. G. Wang, L. Chen, C. Cai, Y. Li, and Y. Zhang, Band insulator to Mott insulator transition in 1T-TaS$_2$, Nat. Commun. **11**, 4215 (2020).

[19] F. J. Di Salvo, B. G. Bagley, J. M. Voorhoeve, and J. V. Waszczak, Preparation and properties of a new polytype of tantalum disulfide (4Hb-TaS$_2$), J. Phys. Chem. Solids **34**, 1357 (1973).

[20] A. H. Thompson, F. R. Gamble, and R. F. Koehler, Jr., Effects of intercalation on electron transport in tantalum disulfide, Phys. Rev. B **5**, 2811 (1972).

[21] P. Coleman, Heavy fermions: Electrons at the edge of magnetism, *Handbook of Magnetism and Advanced Magnetic Materials* (Wiley-Interscience, 2007).

[22] S. Ran, C. Eckberg, Q.-P. Ding, Y. Furukawa, T. Metz, S. R. Saha, I.-L. Liu, M. Zic, H. Kim, J. Paglione *et al.*, Nearly ferromagnetic spin-triplet superconductivity, Science **365**, 684 (2019).

[23] Arushi, D. Singh, A. D. Hillier, M. S. Scheurer, and R. P. Singh, Time-reversal symmetry breaking and multigap superconductivity in the noncentrosymmetric superconductor La$_7$Ni$_3$, Phys. Rev. B **103**, 174502 (2021).

[24] E. Persky, A. Kanigel, and B. Kalisky (private communication).

[25] D. F. Agterberg, P. M. R. Brydon, and C. Timm, Bogoliubov Fermi Surfaces in Superconductors with Broken Time-Reversal Symmetry, Phys. Rev. Lett. **118**, 127001 (2017).

[26] A. A. Abrikosov and L. P. Gor'kov, Contribution to the theory of superconducting alloys with paramagnetic impurities, Zh. Eksp. Teor. Fiz. **39**, 1781 (1960).

[27] S. Skalski, O. Betbeder-Matibet, and P. R. Weiss, Properties of superconducting alloys containing paramagnetic impurities, Phys. Rev. **136**, A1500 (1964).

[28] M. A. Woolf and F. Reif, Effect of magnetic impurities on the density of states of superconductors, Phys. Rev. **137**, A557 (1965).

[29] A. J. Millis, S. Sachdev, and C. M. Varma, Inelastic scattering and pair breaking in anisotropic and isotropic superconductors, Phys. Rev. B **37**, 4975 (1988).

[30] R. M. Fernandes and A. J. Millis, Suppression of Superconductivity by Néel-Type Magnetic Fluctuations in the Iron Pnictides, Phys. Rev. Lett. **110**, 117004 (2013).

[31] K. S. D. Beach, R. J. Gooding, and F. Marsiglio, Reliable Padé analytical continuation method based on a high-accuracy symbolic computation algorithm, Phys. Rev. B **61**, 5147 (2000).

[32] R. M. Fernandes and J. Schmalian, Scaling of nascent nodes in extended-s-wave superconductors, Phys. Rev. B **84**, 012505 (2011).

[33] G. Kresse and J. Furthmüller, Efficient iterative schemes for *ab initio* total-energy calculations using a plane-wave basis set, Phys. Rev. B **54**, 11169 (1996).

[34] G. Kresse and D. Joubert, From ultrasoft pseudopotentials to the projector augmented-wave method, Phys. Rev. B **59**, 1758 (1999).

[35] J. P. Perdew, K. Burke, and M. Ernzerhof, Generalized Gradient Approximation Made Simple, Phys. Rev. Lett. **77**, 3865 (1996).

[36] A. A. Mostofi, J. R. Yates, G. Pizzi, Y.-S. Lee, I. Souza, D. Vanderbilt, and N. Marzari, An updated version of wannier90: A tool for obtaining maximally-localised Wannier functions, Comput. Phys. Commun. **185**, 2309 (2014).

[37] N. Marzari, A. A. Mostofi, J. R. Yates, I. Souza, and D. Vanderbilt, Maximally localized Wannier functions: Theory and applications, Rev. Mod. Phys. **84**, 1419 (2012).

[38] M. S. Dresselhaus, G. Dresselhaus, and A. Jorio, *Applications of Group Theory to the Physics of Solids* (Springer, New York, 2008).

[39] F. Hund, Über den Zusammenhang zwischen der Symmetrie eines Kristallgitters und den Zuständen seiner Elektronen, Z. Phys. **99**, 119 (1936).

[40] H. J. Monkhorst and J. D. Pack, Special points for Brillouin-zone integrations, Phys. Rev. B **13**, 5188 (1976).

[41] J. J. Gao, J. G. Si, X. Luo, J. Yan, Z. Z. Jiang, W. Wang, Y. Y. Han, P. Tong, W. H. Song, X. B. Zhu, Q. J. Li, W. J. Lu, and Y. P. Sun, Origin of the large magnetoresistance in the candidate chiral superconductor $4Hb$-TaS$_2$, Phys. Rev. B **102**, 075138 (2020).

[42] W. Ruan, Y. Chen, S. Tang, J. Hwang, H.-Z. Tsai, R. Lee, M. Wu, H. Ryu, S. Kahn, F. Liou *et al.*, Imaging spinon density modulations in a 2D quantum spin liquid, arXiv:2009.07379.

[43] L. S. Borkowski and P. J. Hirschfeld, Kondo effect in gapless superconductors, Phys. Rev. B **46**, 9274 (1992).

[44] A similar, but not orthonormal, basis with four different $d_{3z^2-r^2}$-like orbitals was discussed in Ref. [45] for $2H$-TaS$_2$.

[45] J. van Wezel, Polar charge and orbital order in $2H$-TaS$_2$, Phys. Rev. B **85**, 035131 (2012).